RSC Advances

PAPER

View Article Online
View Journal | View Issue

Cite this: *RSC Adv.*, 2018, **8**, 35403

Synthesis of $Zn_3(VO_4)_2/BiVO_4$ heterojunction composite for the photocatalytic degradation of methylene blue organic dye and electrochemical detection of H_2O_2†

Muhammad Munir Sajid,[ab] Sadaf Bashir Khan,[b] Naveed Akthar Shad[ac] and Nasir Amin*[a]

Received 2nd September 2018
Accepted 27th September 2018

DOI: 10.1039/c8ra07320a

rsc.li/rsc-advances

In this study, a $Zn_3(VO_4)_2/BiVO_4$ heterojunction nanocomposite photocatalyst was prepared using a hydrothermal route with different molar concentration ratios. The as-synthesized nanophotocatalyst was characterized using XRD, SEM, EDS, XPS, FT-IR, Raman, BET, UV-vis DRS, EPR and PL. The effect of molar ratio on composition and morphology was studied. The as-prepared nanocomposite exhibited excellent photocatalytic response by completely degrading the model pollutant methylene blue (MB) dye in 60 min at molar concentration ratio of 2 : 1. In basic medium at pH 12, the $Zn_3(VO_4)_2/BiVO_4$ nanocomposite degrades MB completely within 45 min. The nanocomposite was also successfully used for the electrochemical detection of an important analyte hydrogen peroxide (H_2O_2). This study opens up a new horizon for the potential applications of $Zn_3(VO_4)_2/BiVO_4$ nanocomposite in environmental wastewater remediation as well as biosensing sciences.

Introduction

In recent years, heterojunction semiconductor photocatalysts have been widely used in many areas, particularly the elimination of toxic chemicals from wastewater[1–3] and electroanalytical applications. Large disposal of dyes from different sectors into water sources creates a threat to the environment. These dyes are major causes of water pollution. Approximately 1 to 20% of the globally produced dye is lost during the dyeing process and expelled in wastewater.[4–6] It is essential to mineralize this contaminated water so that it has no harmful effects on living organisms. Numerous studies have been conducted by researchers, including the use of filtration, electrochemical and precipitation methods, coagulation and adsorption, which are common methods for water remediation. Among these methods, heterogeneous photocatalysis is an advanced oxidation process (AOP) and is widely used to mineralize pollutant water without generating secondary harmful pollutants under light irradiation in the presence of a catalyst.[7,8]

In heterojunctions, the recombination rate reduces and the separation rate of the photogenerated electron–holes speeds up. Hence, heterojunction composites are photocatalytically more active than the individual components. Numerous composites have been reported, such as $NaBiO_3/BiOCl$,[9] Bi_2WO_6/TiO_2,[10] TiO_2/SnO_2,[11] Bi/Bi_2O_3,[12] and $BiVO_4/Bi_2O_3$.[13] It has been agreed from the results of extensive investigations that coupling of two semiconductor photocatalysts would result in better photocatalytic activities.[13–15]

Fabricating heterojunction photocatalysts with different semiconducting materials comprises a frugal action to facilitate the separation of photoexcited electron–hole pairs and achieve better photocatalytic attributes. Several heterojunction photocatalysts have been fabricated by many processes such as sol–gel, co-precipitation,[16] ball milling,[17] and hydrothermal methods.[1,18] From the literature study, we noted that the heterojunction photocatalysts such as $InVO_4/BiVO_4$, $CuO/BiVO_4$, $C_3N_4/BiVO_4$, $BiVO_4/Bi_2S_3$, $BiVO_4/FeVO_4$ and $CaFe_2O_4/Ag_3VO_4$ display higher photocatalytic efficiency when compared with that of single semiconductors.[19–23] When a wide bandgap semiconductor is mixed with a short bandgap semiconductor, charge separation is extended and excellent photocatalytic activity is attained.[1,24]

The energy band gaps of $BiVO_4$ and $Zn_3(VO_4)_2$ are generally 2.4 eV and 3.3 eV, respectively.[25,26] In $BiVO_4$, the conduction band edge is made of Bi 6p orbital and a definite part of V 3d orbital, while the valence band edge is composed of O 2p and V 3d orbital.[27] In the case of $Zn_3(VO_4)_2$, the conduction band edge

[a]*Department of Physics, Government College University Allama Iqbal Road, Faisalabad, 38000, Pakistan. E-mail: nasir786a@yahoo.com*

[b]*The State Key Laboratory for New Ceramics & Fine Processing, School of Materials Science & Engineering, Tsinghua University, Beijing, 100084, China*

[c]*National Institute for Biotechnology and Genetic Engineering (NIBGE), P. O. Box. 577, Jhang Road, Faisalabad, Pakistan*

† Electronic supplementary information (ESI) available. See DOI: 10.1039/c8ra07320a

is made of Zn 3d orbital and V 3d orbital. The valence band edge is composed of O 2p, Zn 3d and V 3d orbitals. Because the energy band gap of $BiVO_4$ < $Zn_3(VO_4)_2$, the electrons can easily transfer from $BiVO_4$ to $Zn_3(VO_4)_2$ and decrease the electron density of the valence band in $BiVO_4$. Similarly, the introduction of $BiVO_4$ decreases the electron density in the conduction band of $Zn_3(VO_4)_2$, which causes conduction band electron transfer to the $Zn_3(VO_4)_2$ surface and reduces recombination of charge pairs.

Thus, from the above literature survey, it is apparent that combination of $BiVO_4$ and $Zn_3(VO_4)_2$ would beneficially increase separation efficiency of electron–hole charges and improve the photocatalytic response of $Zn_3(VO_4)_2/BiVO_4$ heterojunction nanophotocatalyst. To the best of our knowledge, although many studies have been conducted on the $BiVO_4$-based composite for photocatalytic use, we are reporting the first time the use of $Zn_3(VO_4)_2/BiVO_4$ heterojunction composite for the photocatalytic degradation of methylene blue dye as well as the electrochemical detection of hydrogen peroxide molecules. In this study, $Zn_3(VO_4)_2/BiVO_4$ heterojunction composite was prepared through a hydrothermal route. Physical and chemical properties of the as-prepared $Zn_3(VO_4)_2/BiVO_4$ photocatalyst were measured by XRD, XPS, SEM, EDS, FT-IR, Raman, BET, UV-vis DRS, EPR and fluorescence spectrum techniques. The photocatalytic activity of the $Zn_3(VO_4)_2/BiVO_4$ composite photocatalyst was investigated by performing the degradation of methylene blue (MB) dye under visible light. Electrochemical properties (*via* EIS and CV) of the $Zn_3(VO_4)_2/BiVO_4$ composite were also investigated for detecting hydrogen peroxide. This study uncovers the potential of $Zn_3(VO_4)_2/BiVO_4$ nanocomposite for applications in environmental science as well as in biosensor disciplines.

Experimental methods

All the materials were of analytical grade and used without any further purification. The heterojunction composite $Zn_3(VO_4)_2/BiVO_4$ was synthesized by hydrothermal method. Initially, 1 mmol each of $Bi(NO_3)_3 \cdot 5H_2O$ and $Zn(O_2CCH_3)_2$ were dissolved in 100 mL of distilled water. A yellowish coloured solution was obtained on addition of 2 mM NH_4VO_3, following which the solution was stirred for an hour. pH was adjusted to 10 using 1 M NaOH solution. The solution was transferred to a 100 mL Teflon-lined stainless-steel autoclave and subjected to hydrothermal treatment at 200 °C for 48 h. After completing the reaction, the autoclave was cooled naturally and the precipitate was collected and washed numerous times with ethanol and distilled water to remove the surface-bound impurities. Then, the product was dried at 80 °C overnight. To check the effect of different concentrations on the crystallinity, morphology, and photocatalytic and electrochemical sensing properties, $Zn_3(VO_4)_2/BiVO_4$ heterojunction was also prepared at different mole ratios without changing other parameters.

Characterization of $Zn_3(VO_4)_2/BiVO_4$

X-ray diffraction (XRD) was executed on a Bruker D_8 Advance diffractometer using monochromatic Cu Kα (l 1/4 0.15418 nm) radiation with a scanning speed of 2θ min^{-1}. The structure, morphology and size of the particles were examined using a field emission scanning electron microscope (FESEM, Hitachi-S5500) equipped with an energy dispersive X-ray spectroscope (EDS). FT-IR spectra were recorded by an FT-IR spectrometer (Nicolet iS50) from 400 to 4000 cm^{-1}. Raman analysis was preformed through LabRAM HR Evolution (HORIBA Scientific) using 532 nm laser as the excitation source at room temperature. Brunauer–Emmett–Teller (BET) surface area of the products was analyzed by recording an N_2 adsorption–desorption isotherm curve at 77.55 K using a Micromeritics ASAP 2010 system. Before N_2 adsorption measurements, the samples were degassed at 180 °C. A multipoint BET method was used to calculate the surface area. For photoluminescence (PL), the 325 nm line of a He-Cd laser was utilized as the excitation source at room temperature using a Hitachi luminescence spectrometer (F-4500). Electronic paramagnetic resonance (EPR) analysis was performed on an ESR-JES-FA 2010 spectrometer. UV-vis-NIR diffuse reflectance (DRS) measurements were executed on a UV/vis/NIR spectrometer (Perkin Elmer, Lambda-35).

Photocatalytic activity

To test the photocatalytic responses of powdered $Zn_3(VO_4)_2/BiVO_4$, the samples were illuminated under a xenon lamp of accumulative intensity of 300 W to degrade MB under visible-light irradiation; the distance between the reactor and the lamp was 30 cm. For the kinetics study, the dye solutions with fixed concentrations (150 mL) were prepared and 100 mg of the as-synthesized $Zn_3(VO_4)_2/BiVO_4$ was mixed in each dye solution. The obtained solutions were stirred vigorously for 15 min in the dark and illuminated under visible light. Before starting the experiment, solutions were maintained at pH of about 8. The final solutions were centrifuged (10 000 rpm for 5 min) and the nitrogen cooling system HX-DC1006 was employed throughout the experiment to avoid any thermal degradation and to maintain the temperature at 0 °C. Degradation of the dye solutions was analyzed using Perkin Elmer lambda 35 UV/vis spectrometer in the spectral range of 400–800 nm.

Sensor measurement

The electrochemical study was performed on a Chi-760D electrochemical workstation using a three-electrode scheme with a glassy carbon electrode (GCE) applied in this study for electrode modification. Initially, 0.5 mg of $Zn_3(VO_4)_2/BiVO_4$ was dispersed in 1 mL deionized water. Then, 10 μL of this dispersed nanomaterial was drop casted on GCE and dried in the oven at 60 °C for 2–3 min. Then, 2–3 μL of 5% Nafion was added on the coated GCE and dried. All the solutions for sensing element measurements were prepared in deionized water and the involved concentrations were attained by suitable dilution of separate stock solutions. $Zn_3(VO_4)_2/BiVO_4$-modified glassy electrode was employed as the working electrode, a glassy carbon rod was used as the counter electrode and Ag/AgCl electrode was used as the reference electrode. Prior to each electrochemical measurement, the electrolyte solution was degassed with nitrogen gas for 3 min.

Electrochemical impedance spectroscopy (EIS) was performed at an amplitude of 0.01 V in the frequency range of 0.1 Hz to 4000 Hz. Cyclic voltammetry (CV) curves were measured in the potential range of −1.0 V to +1.0 V at a potential scan rate of 0.05 V s^{-1} (except for the effect of scan rate) in a mixed solution of 0.1 M electrolyte and H_2O_2 at different concentrations. All measurements were performed at ambient temperature.

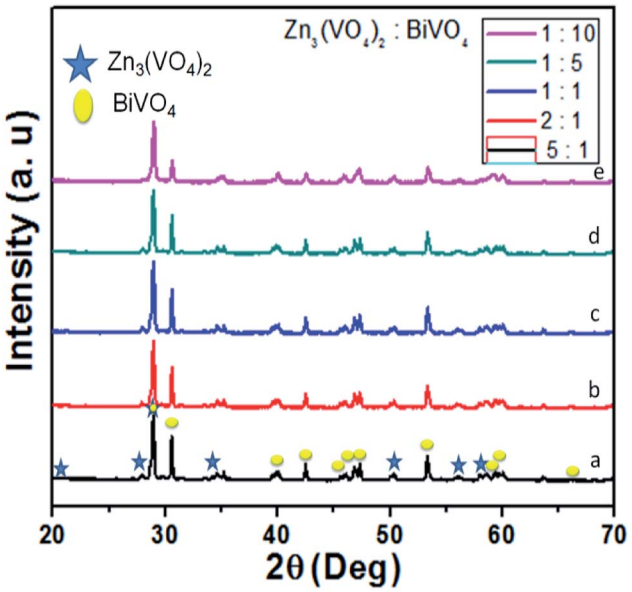

Fig. 1 XRD spectra of $Zn_3(VO_4)_2/BiVO_4$ heterojunction composites at different mole ratios: (a) 5 : 1, (b) 2 : 1, (c) 1 : 1, (d) 1 : 5, and (e) 1 : 10.

Result and discussion

Fig. 1 shows the XRD diffraction patterns for the phase structures of the as-synthesized $Zn_3(VO_4)_2/BiVO_4$ at various concentration ratios. All the XRD diffraction peaks of $Zn_3(VO_4)_2/BiVO_4$ belong to pure $Zn_3(VO_4)_2$ (JCPD card 19-1468) and $BiVO_4$ (JCPD card 75-1867). Hence, the pattern of $Zn_3(VO_4)_2/BiVO_4$ heterojunction photocatalyst compound exhibited characteristic diffraction peaks from both $BiVO_4$ and $Zn_3(VO_4)_2$ crystalline phases, verifying that $Zn_3(VO_4)_2/BiVO_4$ composite was synthesized with success by a facile hydrothermal route at varied mole ratios. It can be seen that as the $BiVO_4$ ratio increases, the $Zn_3(VO_4)_2$ peaks diminish due to broadening of the $BiVO_4$ peaks.

The morphology of the as-synthesized $Zn_3(VO_4)_2/BiVO_4$ heterojunction was characterized by FESEM. $Zn_3(VO_4)_2/BiVO_4$ nanoparticles and nanorods with high yield are observed, as shown in Fig. 2(a–e). It was noticed that as the ratio of $BiVO_4$ increased, particle size also increased, which may be due to aggregation/agglomeration of the particles, as can be seen in Fig. 2(e). For determining the chemical composition, energy dispersive spectroscopy analysis was performed. It can be seen that the main elements within the samples are vanadium, zinc, bismuth, and oxygen at different mole ratios, while the carbon and platinum peaks evolve due to carbon tape and Pt coating.

For obtaining further information on the chemical composition, surface and elemental analysis, X-ray photon spectroscopy (XPS) was used. XPS is a versatile elemental analysis technique for assaying the composition and chemical states of elements.[28] Fig. 3(a) depicts the typical X-ray photoelectron

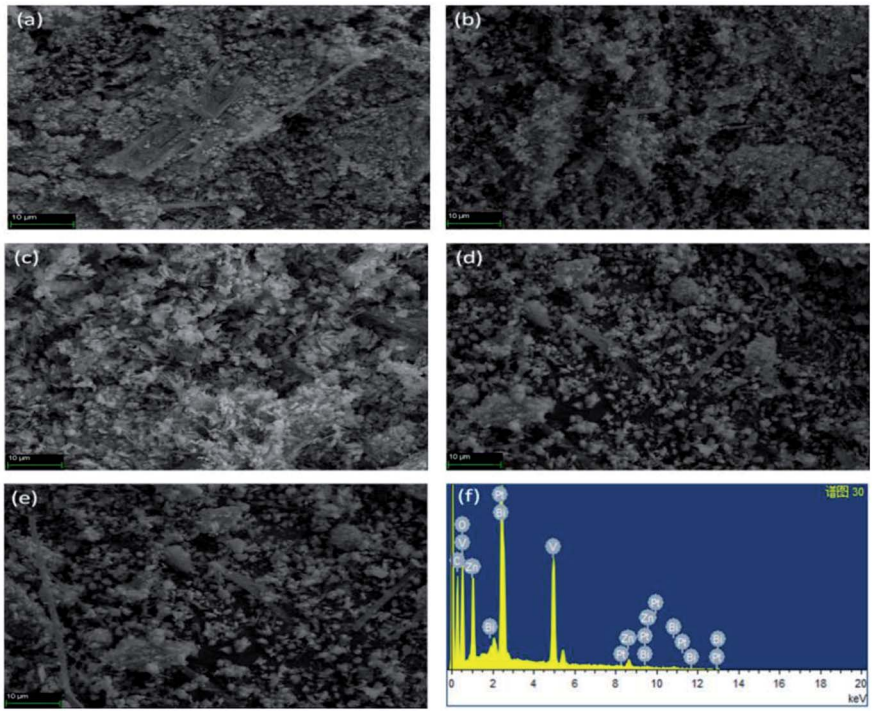

Fig. 2 SEM images of $Zn_3(VO_4)_2/BiVO_4$ composite heterojunction photocatalyst at different mole ratios: (a) 5 : 1, (b) 2 : 1, (c) 1 : 1, (d) 1 : 5, and (e) 1 : 10 and (f) EDS analysis of $Zn_3(VO_4)_2/BiVO_4$ composite at mole ratio 1 : 1.

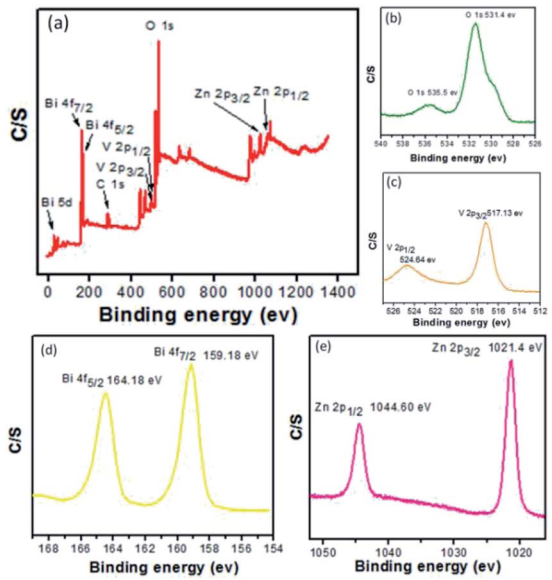

Fig. 3 XPS spectra of as-prepared $Zn_3(VO_4)_2/BiVO_4$ samples at mole ratio 2 : 1. (a) Total survey, (b) O 1s, (c) V 2p, (d) Bi 4f, and (e) Zn 2p.

spectrum of $Zn_3(VO_4)_2/BiVO_4$, which is composed of O, V, Bi, and Zn. XPS analysis of the $Zn_3(VO_4)_2/BiVO_4$ nanocomposite shows two O 1s peaks located at 531.4 and 535.5 eV (Fig. 3(b)), indicating two different forms of O in the sample, which can be assigned to oxygen vacancies related to –OH group and molecular water adsorbed on the surface, respectively. The doublet peaks of V $2p_{3/2}$ and V $2p_{1/2}$ were detected at 517.13 and 524.64 eV, respectively (Fig. 3(c)). Fig. 3(d) shows the XPS peaks at 159.18 and 164.18 eV, belonging to Bi $4f_{7/2}$ and Bi $4f_{5/2}$. In Fig. 3(e), the Zn 2p spectrum presents two main peaks for $2p_{1/2}$ and $2p_{3/2}$ at 1021.4 and 1044.60 eV, respectively. The XPS analyses of the composites with ratios of 5 : 1 and 1 : 10 are given in Fig. S1 (ESI).† The XPS results revealed the suggested formation of $Zn_3(VO_4)_2/BiVO_4$, which confirms the previous XRD results.

Fourier-transform infrared (FT-IR) spectrum of the $Zn_3(VO_4)_2/BiVO_4$ composite at mole ratio of 2 : 1 shows a strong absorption in the range of 400–950 cm^{-1}. The absorption bands at 473, 728 and 741 cm^{-1} belong to $BiVO_4$. The bands at 446, 901, and 931 cm^{-1} correspond to $Zn_3(VO_4)_2$. A weak absorption band at 473 cm^{-1} was assigned to symmetric bending of VO_4^{3-}, while a broad and strong absorption band at 741 cm^{-1} was assigned to the asymmetric stretching of VO_4^{3-}. The peak at 446 cm^{-1} indicates stretching vibration mode of the Zn–O band. The vibration bands at 901 and 931 cm^{-1} are attributed to VO_4 vibration mode in the network. The absorption band at 728 cm^{-1} indicates the stretching vibration of the Bi–V band.[29–32] Fig. 4(b) shows the Raman spectrum of $Zn_3(VO_4)_2/BiVO_4$ at 2 : 1 ratio. The Raman spectrum reflects bands at around 116, 199, 210, 334, 692, and 815 cm^{-1} for all samples. The peaks at 116 and 199.6 cm^{-1} arise from Zn–O vibration, the peaks at 210, 334, and 692 cm^{-1} arise from Bi–V vibration, and the peak at 815 cm^{-1} is attributed to V–O vibration.[31,33,34] Raman spectrum of the product is in good agreement with the crystal structure of $Zn_3(VO_4)_2/BiVO_4$.

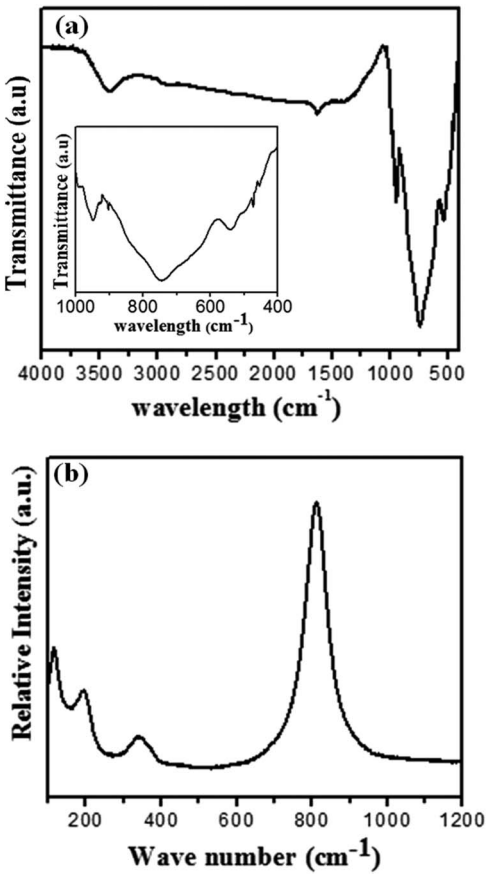

Fig. 4 (a) FT-IR spectrum of $Zn_3(VO_4)_2/BiVO_4$, (inset) high-resolution spectrum from 400 to 1000 cm^{-1}; (b) Raman spectrum of as-prepared $Zn_3(VO_4)_2/BiVO_4$ at mole ratio 2 : 1.

Fig. 5(a) shows the N_2 adsorption–desorption isotherm of $Zn_3(VO_4)_2/BiVO_4$ at 2 : 1 mole ratio. The Brunauer–Emmett–Teller (BET) surface area of 40.46 $cm^2\ g^{-1}$, pore volume of 0.122 $cm^3\ g^{-1}$ and pore diameter of 1.685 nm were calculated from experimental data. The large surface area and volume correspond to highly reactive sites, resulting in enhanced photocatalytic activity of the material.[35] N_2 adsorption isotherms at different ratios of $Zn_3(VO_4)_2/BiVO_4$ were obtained and analyzed, corresponding to the H_3 hysteresis loop, which indicated aggregation of the sample particles to form self-assembled nanoparticles, as shown in Fig. S2 (ESI).† The shapes of all the $Zn_3(VO_4)_2/BiVO_4$ sample isotherms resembled type H_3 loops, indicating aggregation of sample particles to form self-assembled plate-like and rod-like particles.

Energy band gap is an important parameter of semiconductor materials. The UV-visible spectrum of the $Zn_3(VO_4)_2/BiVO_4$ nanophotocatalyst was recorded and the band gap, as depicted in Fig. 5(b), was calculated by the Tauc relation (1):

$$(\alpha h\nu) = A(h\nu - E_g)^n \quad (1)$$

where α = absorption coefficient, A = constant, and $n = 1/2$ was used for direct band gap material. E_g value was calculated to be 2.89 eV for $Zn_3(VO_4)_2/BiVO_4$.

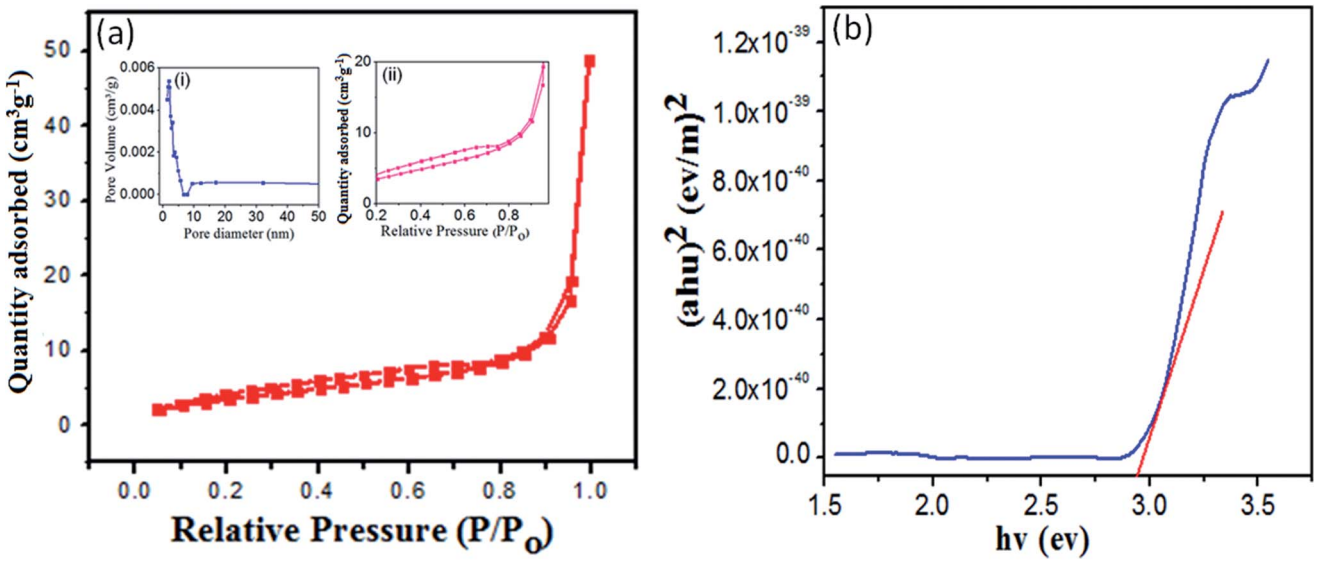

Fig. 5 (a) N_2 adsorption–desorption isotherm distribution curves for $Zn_3(VO_4)_2/BiVO_4$ at 2 : 1 mole ratio, insets (i) differential pore size distribution curve from Barrett–Joyner–Halenda (BJH) method and (ii) high resolution N_2 adsorption–desorption isotherm at 2 : 1 mole ratio; (b) Tauc plot for $Zn_3(VO_4)_2/BiVO_4$ composite at 2 : 1 mole ratio.

Fig. S3 (ESI†) shows the changes in the visible (UV-vis) spectra during the photodegradation process of MB dye in aqueous $Zn_3(VO_4)_2/BiVO_4$ solution under visible light irradiation. The chemical structure of MB is shown in Fig. S4 (ESI†) and details about concentration are given in ESI.† It was noted that at the ratio of 2 : 1 of $Zn_3(VO_4)_2/BiVO_4$ heterogeneous photocatalyst, nearly the entire dye degraded in 90 min.

Concentration changes *versus* irradiation time and the degradation efficiency graph are shown in Fig. 6. When visible light illuminates the solution, the active species, namely, hydroxyl radicals, holes, $^{-}O_2$ and $\cdot O_2$ are generated during the photocatalytic degradation reaction. The formation of $OH^{\cdot}$ radicals is much lower than $O_2^{\cdot}$ formation. However, the hydroxyl radical is a highly active and non-selective oxidant agent species for degradation, which leads to mineralization of organic chemicals.[36–41]

Degradation efficiency was determined by the following equation:

$$\text{Degradation efficiency (\%)} = (C_o - C_t)/C_o \quad (2)$$

where C_o is the initial concentration at time t_o and C_t is the concentration at any time t. Fig. 6(a and b) indicate the degradation efficiency at the same dose as the catalyst.

The mechanism of photocatalytic MB dye solution degradation by the $Zn_3(VO_4)_2/BiVO_4$ nanophotocatalyst in visible light can be presented through the following equations:

$$Zn_3(VO_4)_2/BiVO_4 + h\nu \rightarrow e^- + h^+ + Zn_3(VO_4)_2/BiVO_4 \quad (3)$$

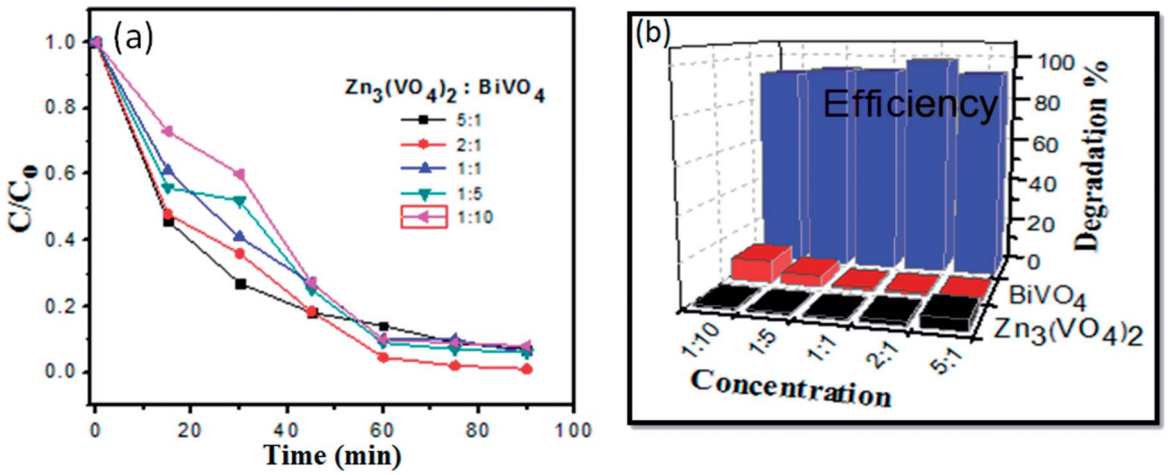

Fig. 6 (a) Concentration changes (C/C_o) of MB dye as function of irradiation time in presence of photocatalyst at same quantity but different mole ratios; (b) bar graph of efficiency at different mole ratios.

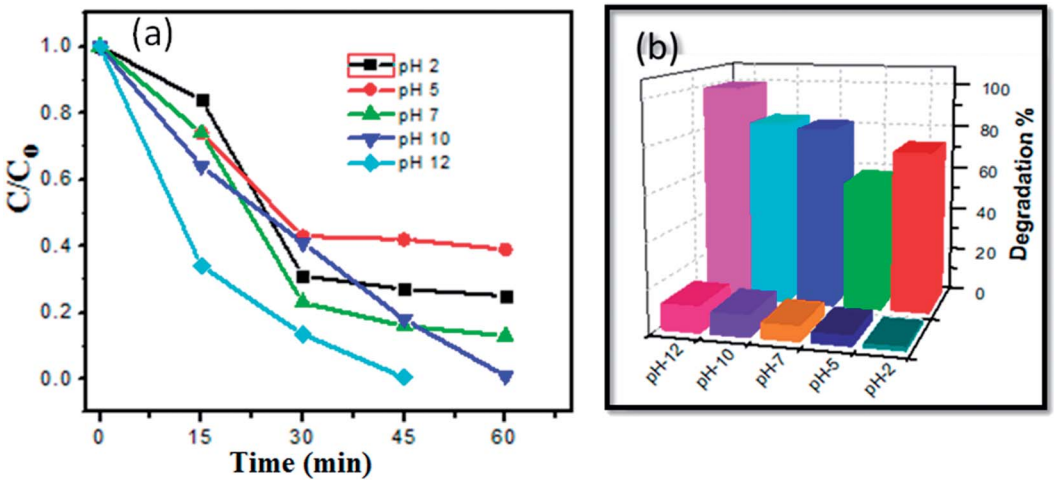

Fig. 7 (a) Concentration changes (C/C_o) of MB dye as function of irradiation time in presence of photocatalyst at different pH; (b) bar graph of efficiency of $Zn_3(VO_4)_2/BiVO_4$ nanophotocatalyst at different pH values.

Oxidation occurs at $BiVO_4$ surfaces:

$$h^+ + H_2O \rightarrow \cdot OH + H^+ \quad (4)$$

$$2h^+ + 2H_2O \rightarrow 2H^+ + H_2O_2 \quad (5)$$

Reduction reaction occurs at $Zn_3(VO_4)_2$:

$$e^- + O_2 \rightarrow \cdot O_2^- \quad (6)$$

When visible light interacts with the methylene blue dye and $Zn_3(VO_4)_2/BiVO_4$ photocatalyst solution, the electron moves from $BiVO_4$ to $Zn_3(VO_4)_2$, while the hole of $Zn_3(VO_4)_2$ moves to the valence band (V_B) of $BiVO_4$. Then, oxidation reaction occurs at V_B of $Zn_3(VO_4)_2/BiVO_4$, where positive holes react with water and form the hydroxyl radical ($\cdot OH$) radical. Reduction occurs at conduction band (C_B) of $BiVO_4$, where negative electron (e^-) produces superoxide radical ($\cdot O_2$) by reacting with dissolved oxygen. Pseudo-first order equation specified below was applied to extract the reaction kinetics of the organic dye:

$$\ln(C/C_o) = -kt \quad (7)$$

where C is the concentration of the dye at time "t", C_o is concentration at time "t_o" and k is the pseudo-first order rate constant. The degradation rate constant k for MB over $Zn_3(VO_4)_2/BiVO_4$ under visible light irradiation applying pseudo first order was calculated to be 0.01522, 0.01922, 0.01296, 0.01325 and 0.01076 min^{-1} at ratios 5 : 1, 2 : 1, 1 : 1, 1 : 5, and 1 : 10, respectively. It was observed that dye solution with 2 : 1 ratio of $Zn_3(VO_4)_2/BiVO_4$ exhibited the highest photodegradation efficiency, as shown in Fig. 6.

Effect of pH was also examined at different values (2, 5, 7, 10 and 12), as illustrated in Fig. S5 (ESI).† We observed that at pH 12, the MB aqueous solution was totally degraded in 45 min due to the excess amount of $OH^\bullet$ radicals. Hydroxyl radical is a strong oxidant agent. Thus, degradation *via* $O_2^\bullet$ along with $OH^\bullet$ resulted in nearly total (99.6%) degradation MB within 45 min. During the photocatalytic degradation process, a new absorption band and peak shift were observed, which could be due to decomposition of the benzene ring in the dye. Concentration changes *versus* irradiation time and degradation efficiency at various pH values are shown in Fig. 7 (Tables 1 and 2).

Table 1 Effect of pH on MB dye solution of $Zn_3(VO_4)_2/BiVO_4$ in 45 min

pH	Degradation efficiency%
2	73
5	58
7	82
10	84
12	99.6

Table 2 Degradation comparison of methylene blue dye using $Zn_3(VO_4)_2/BiVO_4$ composite with other nanomaterial photocatalysts

Catalyst	Efficiency%	Light source	Time (min)	Reference
ZnS	88	Visible light	90	46
V_2O_3/CNT/TiO_2	70	Visible light	120	47
$BiVO_4/TiO_2$	86	Visible light	120	48
CuO–$BiVO_4$	92	Visible light	300	49
P-25, Degussa	89	Visible light	120	50
$Zn_3(VO_4)_2/BiVO_4$	98.91	Visible light	90	Present work
$Zn_3(VO_4)_2/BiVO_4$ at pH 12	99.6	Visible light	45	Present work

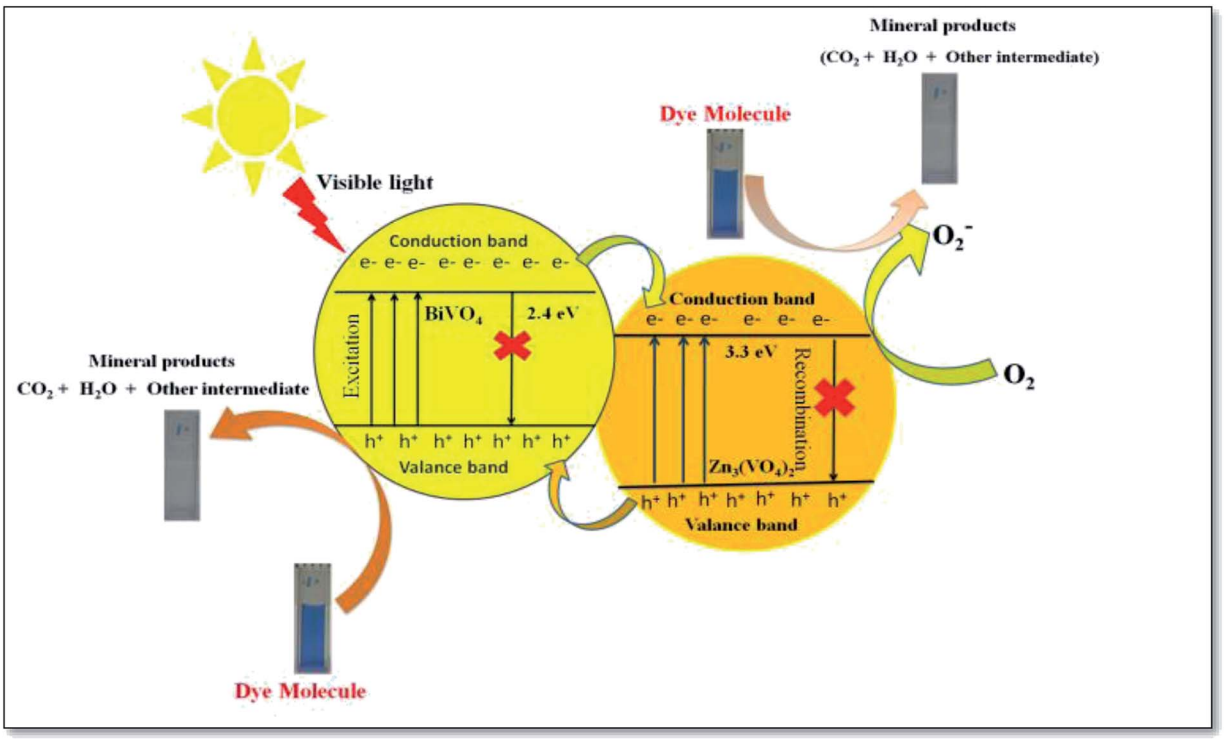

Fig. 8 Reaction mechanism of methylene blue photodegradation over $Zn_3(VO_4)_2/BiVO_4$ nanocomposite under visible light.

The superoxide radical and hydroxide radical oxidize the toxic $C_{16}H_{18}ClN_3S$ dye molecule and decompose it into harmless or non-toxic molecules, namely, CO_2, H_2O, NO_2 and benzene byproducts, as indicated below (Fig. 8).

$$C_{16}H_{18}ClN_3S + (OH^{\bullet}, \cdot O_2^{-}) \rightarrow H_2O + CO_2 + NO_2 + SO_2 + C_6H_6 \quad (8)$$

The photoluminescence (PL) spectrum exposes the recombination rate and charge (electron, hole) separation within the semiconductor nanophotocatalyst. Higher PL intensity indicates that there is a higher rate of recombination, which causes lower degradation efficiency.[42,43] In the PL spectra, the lower intensity indicates the reduced and controlled recombination, which results in the effective electron–hole transfer over the photocatalyst surface and allows superior degradation of contaminants, thus

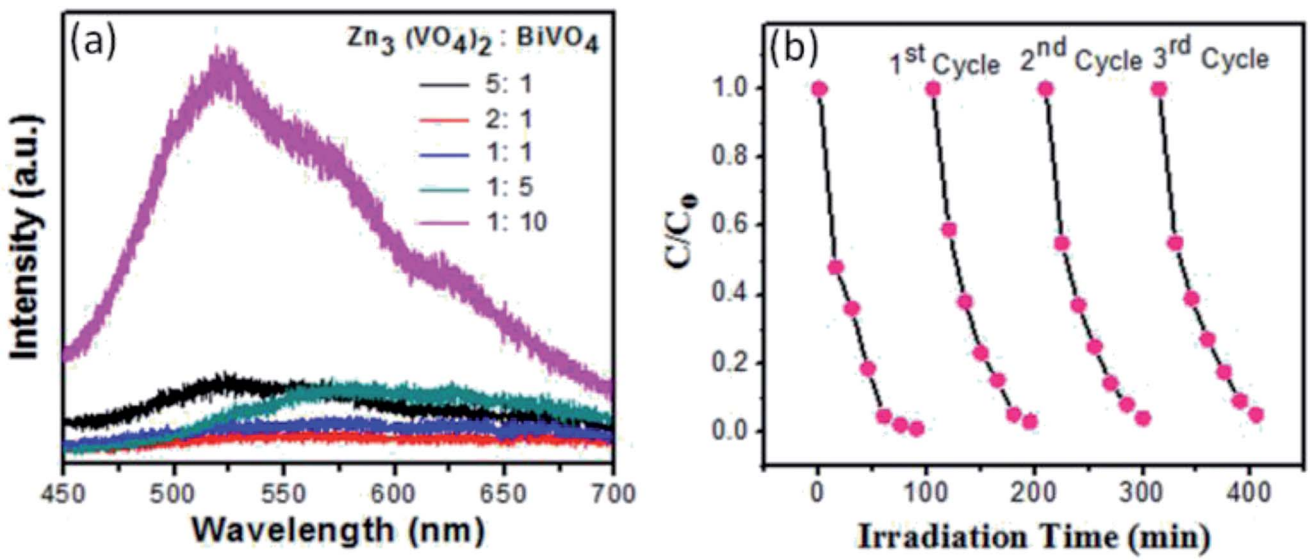

Fig. 9 (a) PL spectra of $Zn_3(VO_4)_2/BiVO_4$ composite at different concentrations; (b) stability of $Zn_3(VO_4)_2/BiVO_4$ for degradation of methyl blue dye under visible light.

increasing photocatalyst efficiency.[44,45] Moreover, the reusability of $Zn_3(VO_4)_2/BiVO_4$ nanophotocatalyst at the ratio of 2 : 1 was checked, as shown in Fig. 9(b). The photolytic activity test was repeated three times and the sample showed good stability.

On the basis of the earlier mentioned literature study, when the electron entered the conduction band of $Zn_3(VO_4)_2$, it generates oxygen from the compound, which made bases for decomposition of MB dye. Hydroxyl radicals were also produced by the reaction of $\cdot O_2$ radicals with H^+ ions and h^+ holes with H_2O. It was noticed that no electron paramagnetic resonance (EPR) signal was found when the reaction was performed in the dark, whereas the signals with intensities corresponding to the characteristic peaks of DMPO–OH˙ adducts were observed during the reaction process in the EPR experiment. However, no peaks of DMPO–$\cdot O_2$ were observed. As shown in Fig. 10, the four characteristic peaks of DMPO–OH˙ radical (1 : 2 : 2 : 1 quartet pattern) were observed by irradiation of the $Zn_3(VO_4)_2/BiVO_4$ heterojunction nanocomposite solution under visible light. Decay of MB dye by the generated oxidant species can be described by the following equation.

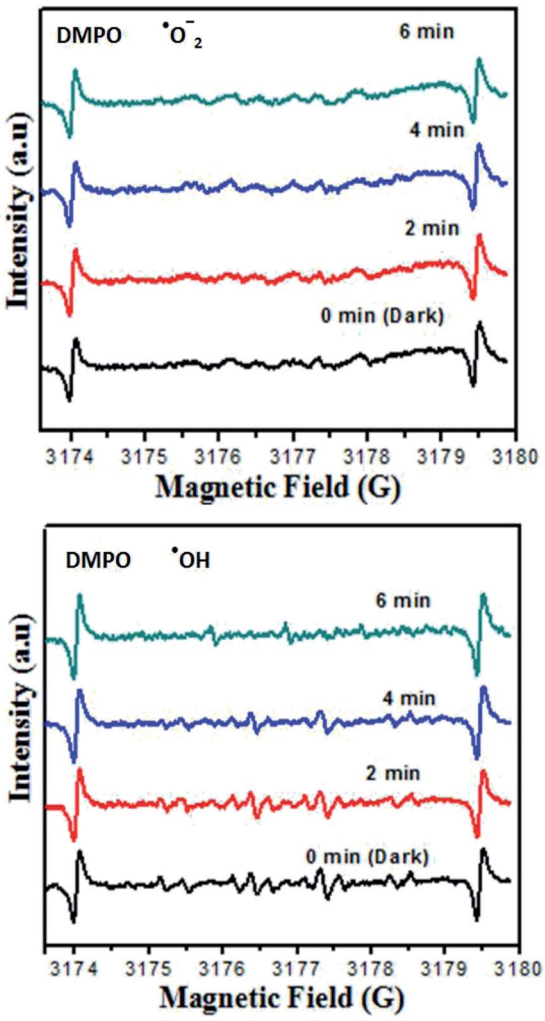

Fig. 10 DMPO spin trapping EPR spectra for DMPO–$\cdot O_2^-$ and DMPO–$\cdot OH^-$ under visible light irradiation with $Zn_3(VO_4)_2/BiVO_4$ photocatalyst.

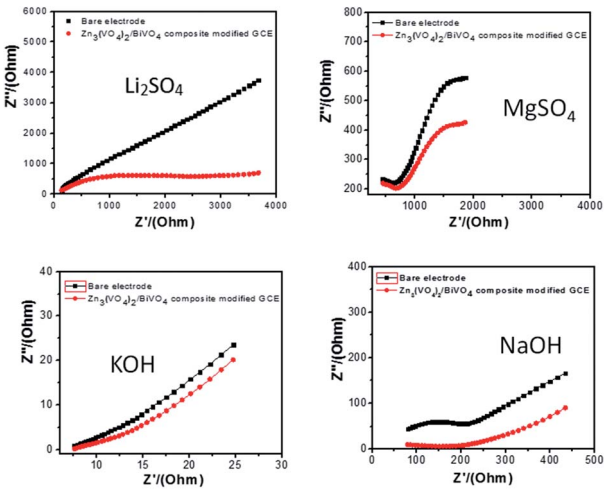

Fig. 11 Electrochemical impedance spectroscopy of bare and modified $Zn_3(VO_4)_2/BiVO_4$ nanocomposite GCE in different electrolytes: (a) 0.1 M Li_2SO_4, (b) 0.1 M $MgSO_4$, (c) 0.1 M KOH and (d) 0.1 M NaOH.

$$MB + OH^{\bullet} \rightarrow \text{decomposed compounds} \quad (9)$$

Electrochemical impedance spectroscopy (EIS) Nyquist plot analysis represents a flexible tool for conductivity analysis, surface psychoanalysis, and electron transfer analysis.[51] As shown in Fig. 11, it is clear that the impedance spectrum is either semicircular or nearly circular at higher ac frequency and a line at low modulation ac frequency. The Nyquist circle diameter of $Zn_3(VO_4)_2/BiVO_4$ is much lower than that of bare glassy carbon electrode, indicating that electron transfer in the $Zn_3(VO_4)_2/BiVO_4$ composite is much sharper than that in the bare GCE and resulting in decreasing resistance.

Hydrogen peroxide (H_2O_2) is a pale-blue liquid and is among the most important analytes. H_2O_2 is used in several areas for food processes, environmental analysis, fabric manufacture, pharmaceuticals, medical diagnostics, clinical laboratories, antiseptic and disinfecting agents, powerful oxidizing agents and is also involved in several biological events as a by-product of oxidases. Higher concentrations of H_2O_2 (>50 μM) can cause stomach irritation and tissue burns. However, low levels of H_2O_2 affect the physiology of human fibroblasts. Hence, the development of an accurate, sensitive, highly reliable as well as low cost sensitizer for hydrogen peroxide (H_2O_2) is desirable. In this scenario, electrochemical sensors with fast response, superior selectivity, high sensitivity, ease of operation and low cost are the optimal option for actualizing the accurate detection of hydrogen peroxide.[52–54] Cyclic voltammetry was employed for the measurement and detection of hydrogen peroxide analyte for $Zn_3(VO_4)_2/BiVO_4$ nanocomposite material. Cyclic voltammetry showed the response of bare electrode and glassy carbon modified electrode in both presence and absence of 0.5 mM hydrogen peroxide at a scan rate of −1 to 1 V s^{-1}, as shown in Fig. 12(a).

In Li_2SO_4 solution (Fig. 12(a)), bare GCE gives one oxidation and one reduction peak located at 0.18 V and −0.43 V, respectively, while the modified $Zn_3(VO_4)_2/BiVO_4$ glassy carbon

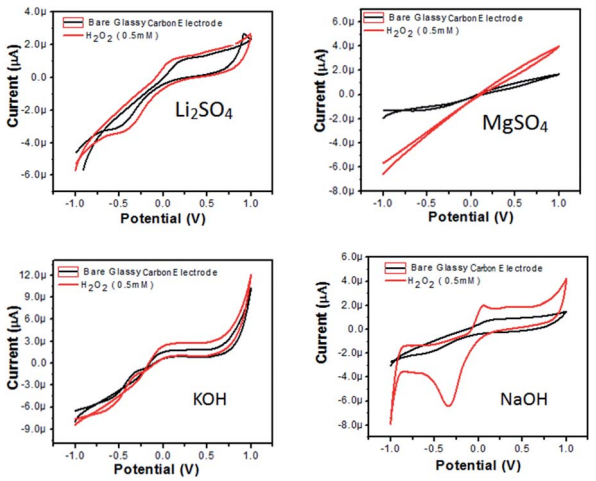

Fig. 12 CVs of $Zn_3(VO_4)_2/BiVO_4$ modified GCE in (a) 0.1 M Li_2SO_4, (b) 0.1 M $MgSO_4$, (c) 0.1 M KOH and (d) 0.1 M NaOH solution in absence and presence of 0.5 mM H_2O_2 at scan rate 50 mV s^{-1}.

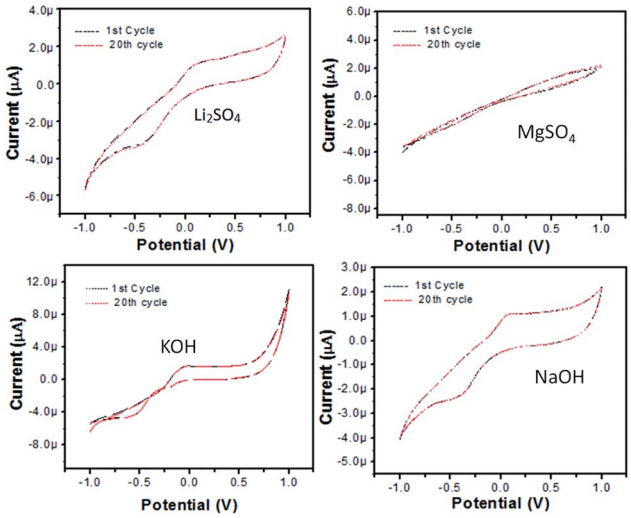

Fig. 13 CVs of $Zn_3(VO_4)_2/BiVO_4$ modified GCE in mixed (a) 0.1 M Li_2SO_4, (b) 0.1 M $MgSO_4$, (c) 0.1 M KOH, (d) 0.1 M NaOH and hydrogen peroxide (0.5 mM) solution at scan rate 50 mV s^{-1}, cycling for 1st and 20th time.

electrode exhibits enhanced current and a CV voltammogram with one oxidation and one reduction peak located at 0.07 V and −0.37 V, respectively. In $MgSO_4$, the bare electrode and modified glassy carbon electrode solution did not show any oxidation peak in either absence or presence of H_2O_2. However, enhanced current was observed, which shows that semiconductor material has the potential to change the current intensity (Fig. 12(b)). In KOH solution (Fig. 12(c)), again no oxidation or reduction peak was observed for either bare GCE or modified $Zn_3(VO_4)_2/BiVO_4$ nanocomposite GCE. However, there was enhanced current intensity in the case of the modified nanocomposite GCE, indicating the potential for changing the current. In NaOH solution (Fig. 12(d)), the bare electrode shows one oxidation and reduction peak at 0.15 and −0.5 V, respectively, while the modified $Zn_3(VO_4)_2/BiVO_4$ nanocomposite GCE shows enhanced current intensity as well as one oxidation and reduction peak at 0.049 and −0.34 V, respectively. From the above-detailed CV spectra, the possibility of using $Zn_3(VO_4)_2/BiVO_4$ as sensor was evidenced.

For long-term stability confirmation, we stored the modified $Zn_3(VO_4)_2/BiVO_4$ composite GCE for three weeks at ambient temperature and then used it for sensing H_2O_2. We found that the modified $Zn_3(VO_4)_2/BiVO_4$ could detect H_2O_2 although there was a decrease in current from the first-day values, but its retention of reproducibility after twenty measurements shows a minor relative standard deviation from the original value, as shown in Fig. 13. Hence, the modified $Zn_3(VO_4)_2/BiVO_4$ composite GCE shows stability and reproducibility for H_2O_2 electrochemical determination.

Conclusions

A $Zn_3(VO_4)_2/BiVO_4$ heterogeneous nano-photocatalyst was prepared through an autoclave hydrothermal method using bismuth nitrate pentahydrate ($Bi(NO_3)_3 \cdot 5H_2O$) and zinc acetate ($Zn(O_2CCH_3)_2$) as bismuth and zinc ion sources, respectively, and ammonia metavanadate (NH_4VO_3) as the vanadium ion source. The as-prepared nanocomposite was characterized by X-ray diffraction (XRD), scanning electron microscopy (SEM), energy dispersive X-ray spectroscopy (EDX), X-ray photoelectron spectroscopy (XPS), FT-IR, Raman, Brunauer–Emmett–Teller (BET), photoluminescence (PL), and EPR. For determining electrochemical response, cyclic voltammetry (CV) and electrochemical impedance spectroscopy (EIS) were performed. $Zn_3(VO_4)_2/BiVO_4$ nanocomposites were investigated for determining the activity of the nanophotocatalyst by photocatalytic degradation of methylene blue (MB) toxic dye under visible light irradiation. The catalyst showed excellent results and decomposed the toxic dye into mineral products (CO_2, H_2O and other intermediate product that are not/less harmful) in 45 min at pH 12. The material was also studied for electrochemical detection of an important analyte hydrogen peroxide (H_2O_2) and showed good results. This study indicates the potential of $Zn_3(VO_4)_2/BiVO_4$ nanocomposites for application in environmental remediation and biosensor sciences.

Funding detail

The authors did not receive financial support for this work from any agency.

Conflicts of interest

There are no conflicts of interest to declare.

Acknowledgements

All the experiments were performed at Government college university Faisalabad, Pakistan. SEM, EDX, XPS, BET, Raman, PL and ESR techniques were supported by Dr Zhengjun Zhang, Advanced Key Laboratory for New Ceramics, School of Materials Science & Engineering, Tsinghua University, Beijing, China, 100084.

Notes and references

1 J. Li, W. Zhao, Y. Guo, Z. Wei, M. Han, H. He, S. Yang and C. Sun, *Appl. Surf. Sci.*, 2015, **351**, 270–279.
2 Y.-R. Jiang, H.-P. Lin, W.-H. Chung, Y.-M. Dai, W.-Y. Lin and C.-C. Chen, *J. Hazard. Mater.*, 2015, **283**, 787–805.
3 G. Shen, L. Pan, Z. Lü, C. Wang, X. Zhang and J.-J. Zou, *Chin. J. Catal.*, 2018, **39**, 920–928.
4 A. Houas, H. Lachheb, M. Ksibi, E. Elaloui, C. Guillard and J.-M. Herrmann, *Appl. Catal., B*, 2001, **31**, 145–157.
5 C. L. Wong, Y. N. Tan and A. R. Mohamed, *J. Environ. Manage.*, 2011, **92**, 1669–1680.
6 F. Han, V. S. R. Kambala, M. Srinivasan, D. Rajarathnam and R. Naidu, *Appl. Catal., A*, 2009, **359**, 25–40.
7 F. Sayılkan, S. Erdemoğlu, M. Asiltürk, M. Akarsu, Ş. Şener, H. Sayılkan, M. Erdemoğlu and E. Arpaç, *Mater. Res. Bull.*, 2006, **41**, 2276–2285.
8 R. Andreozzi, V. Caprio, A. Insola and R. Marotta, *Catal. Today*, 1999, **53**, 51–59.
9 X. Chang, G. Yu, J. Huang, Z. Li, S. Zhu, P. Yu, C. Cheng, S. Deng and G. Ji, *Catal. Today*, 2010, **153**, 193–199.
10 Y. Zhou, F. Krumeich, A. Heel and G. R. Patzke, *Dalton Trans.*, 2010, **39**, 6043–6048.
11 Z. Liu, D. D. Sun, P. Guo and J. O. Leckie, *Nano Lett.*, 2007, **7**, 1081–1085.
12 X. Liu, H. Cao and J. Yin, *Nano Res.*, 2011, **4**, 470–482.
13 M.-L. Guan, D.-K. Ma, S.-W. Hu, Y.-J. Chen and S.-M. Huang, *Inorg. Chem.*, 2010, **50**, 800–805.
14 Z. Wang, B. Huang, Y. Dai, X. Qin, X. Zhang, P. Wang, H. Liu and J. Yu, *J. Phys. Chem. C*, 2009, **113**, 4612–4617.
15 G. Dai, J. Yu and G. Liu, *J. Phys. Chem. C*, 2011, **115**, 7339–7346.
16 M. Baojun, L. Keying, S. Weiguang and L. Wanyi, *Appl. Surf. Sci.*, 2014, **317**, 682–687.
17 S. Chen, S. Zhang, W. Zhao and W. Liu, *J. Nanopart. Res.*, 2009, **11**, 931–938.
18 A. Beltrán, L. Gracia, J. Andrés and E. Longo, *J. Phys. Chem. C*, 2017, **121**, 27624–27642.
19 S. Chen, W. Zhao, W. Liu, H. Zhang, X. Yu and Y. Chen, *J. Hazard. Mater.*, 2009, **172**, 1415–1423.
20 L. Ma, S. Liang, X. L. Liu, D. J. Yang, L. Zhou and Q. Q. Wang, *Adv. Funct. Mater.*, 2015, **25**, 898–904.
21 C. Li, S. Wang, T. Wang, Y. Wei, P. Zhang and J. Gong, *Small*, 2014, **10**, 2783–2790.
22 X. Gao, H. B. Wu, L. Zheng, Y. Zhong, Y. Hu and X. W. D. Lou, *Angew. Chem.*, 2014, **126**, 6027–6031.
23 C. Shifu, Z. Wei, L. Wei, Z. Huaye, Y. Xiaoling and C. Yinghao, *J. Hazard. Mater.*, 2009, **172**, 1415–1423.
24 L. Pan, J. Zhang, X. Jia, Y.-H. Ma, X. Zhang, L. Wang and J.-J. Zou, *Chin. J. Catal.*, 2017, **38**, 253–259.
25 I. Khan, S. Ali, M. Mansha and A. Qurashi, *Ultrason. Sonochem.*, 2017, **36**, 386–392.
26 N. Ahmed, S. Mukhtar, W. Gao and S. Z. Ilyas, *Chin. Phys. B*, 2018, **27**, 033101.
27 S. Yao, K. Ding and Y. Zhang, *Theor. Chem. Acc.*, 2010, **127**, 751–757.
28 J.-M. Wu, Y. Chen, L. Pan, P. Wang, Y. Cui, D. Kong, L. Wang, X. Zhang and J.-J. Zou, *Appl. Catal., B*, 2018, **221**, 187–195.
29 P. Pookmanee, S. Kojinok, R. Puntharod, S. Sangsrichan and S. Phanichphant, *Ferroelectrics*, 2013, **456**, 45–54.
30 P. Pookmanee, S. Kojinok and S. Phanichphant, *Trans. Mater. Res. Soc. Jpn.*, 2014, **39**, 431–434.
31 S. Ni, X. Wang, G. Zhou, F. Yang, J. Wang and D. He, *J. Alloys Compd.*, 2010, **491**, 378–381.
32 R. M. Kakhki and F. Ahsani, *J. Mater. Sci.: Mater. Electron.*, 2018, **29**, 3767–3774.
33 M. Gotić, S. Musić, M. Ivanda, M. Šoufek and S. Popović, *J. Mol. Struct.*, 2005, **744**, 535–540.
34 S. Thalluri, C. Martinez-Suarez, A. Virga, N. Russo and G. Saracco, *Int. J. Chem. Eng. Appl.*, 2013, **4**, 305.
35 M. B. Navas, I. D. Lick, P. A. Bolla, M. L. Casella and J. F. Ruggera, *Chem. Eng. Sci.*, 2018, **187**, 444–454.
36 W. W. Lee, C.-S. Lu, C.-W. Chuang, Y.-J. Chen, J.-Y. Fu, C.-W. Siao and C.-C. Chen, *RSC Adv.*, 2015, **5**, 23450–23463.
37 C.-T. Yang, W. W. Lee, H.-P. Lin, Y.-M. Dai, H.-T. Chi and C.-C. Chen, *RSC Adv.*, 2016, **6**, 40664–40675.
38 S.-Y. Chou, C.-C. Chen, Y.-M. Dai, J.-H. Lin and W. W. Lee, *RSC Adv.*, 2016, **6**, 33478–33491.
39 S.-Y. Chou, W.-H. Chung, L.-W. Chen, Y.-M. Dai, W.-Y. Lin, J.-H. Lin and C.-C. Chen, *RSC Adv.*, 2016, **6**, 82743–82758.
40 F.-Y. Liu, Y.-R. Jiang, C.-C. Chen and W. W. Lee, *Catal. Today*, 2018, **300**, 112–123.
41 D. Zeng, W. Xu, W.-J. Ong, J. Xu, H. Ren, Y. Chen, H. Zheng and D.-L. Peng, *Appl. Catal., B*, 2018, **221**, 47–55.
42 A. Arshad, J. Iqbal, M. Siddiq, Q. Mansoor, M. Ismail, F. Mehmood, M. Ajmal and Z. Abid, *J. Appl. Phys.*, 2017, **121**, 024901.
43 J. Liu, B. Cheng and J. Yu, *Phys. Chem. Chem. Phys.*, 2016, **18**, 31175–31183.
44 C. Shifu, Z. Wei, L. Wei and Z. Sujuan, *J. Sol-Gel Sci. Technol.*, 2009, **50**, 387–396.
45 S. Fatima, S. I. Ali, M. Z. Iqbal and S. Rizwan, *RSC Adv.*, 2017, **7**, 35928–35937.
46 H. Rao, Z. Lu, X. Liu, H. Ge, Z. Zhang, P. Zou, H. He and Y. Wang, *RSC Adv.*, 2016, **6**, 46299–46307.
47 M.-L. Chen and W.-C. Oh, *Int. J. Photoenergy*, 2010, **2010**, 264831.
48 K. Pingmuang, A. Nattestad, J. Chen, W. Kangwansupamonkon and S. Phanichphant, *J. Environ. Sci.*, 2016, **3**, 1–8.
49 A. H. Abdullah, W. T. Peng and M. Z. Hussein, *Malaysian Journal of Analytical Sciences*, 2016, **20**, 1338–1345.
50 X. Li, M. Zou and Y. Wang, *Molecules*, 2017, **22**, 1943.
51 L. Pei, N. Lin, T. Wei, H. Liu and H. Yu, *J. Mater. Chem. A*, 2015, **3**, 2690–2700.
52 M. Liu, Y. X. Yu and W. D. Zhang, *Electroanalysis*, 2017, **29**, 305–311.
53 S. Zeki Bas, C. Cummins, D. Borah, M. Ozmen and M. A. Morris, *Anal. Chem.*, 2017, **90**(2), 1122–1128.
54 Z. Yu, S. Lv, R. Ren, G. Cai and D. Tang, *Microchim. Acta*, 2017, **184**, 799–806.

